Nanoscale

PAPER

View Article Online
View Journal | View Issue

Check for updates

Cite this: *Nanoscale*, 2025, **17**, 8850

Swapping CO_2 electro-reduction active sites on a nickel-based hybrid formed on a "guilty" covalent triazine framework†

Giulia Tuci, *[a] Miriam Moro,[b] Andrea Rossin, [a] Claudio Evangelisti, [c] Lorenzo Poggini,[a,d] Marco Etzi, [e] Enrico Verlato, [f] Francesco Paolucci, [b,f,g] Yuefeng Liu,[h] Giovanni Valenti *[b,g] and Giuliano Giambastiani *[a,d]

A homogeneous and almost monodisperse Ni/CTF^{ph} composite of ultrasmall Ni NPs (~2.2 nm) has been prepared by Metal Vapor Synthesis (MVS) and deposited on a highly porous and high specific surface area covalent triazine network. Metal doping was deliberately carried out on a metal-free system exhibiting superior CO_2RR selectivity towards the challenging CO_2-to-HCOOH electroreduction. Electrochemical studies aimed at shedding light on the CO_2RR performance of the ultimate composite have allowed speculation on the synergistic or exclusive action of the two potentially active phases (N-doped C-network *vs*. Ni NPs). In contrast to the generally exclusive CO_2-to-CO reduction mechanism described for the *state-of-the-art* Ni NP-based CO_2RR electrocatalysts, Ni/CTF^{ph} has unveiled the unprecedented ability of Ni NPs to promote the alternative and more challenging 2e$^-$ CO_2-to-HCOOH reduction pathway, even at moderately reducing potentials (−0.3 V *vs*. RHE).

Received 13th December 2024,
Accepted 26th February 2025

DOI: 10.1039/d4nr05259e

rsc.li/nanoscale

Open Access Article. Published on 27 February 2025. Downloaded on 1/18/2026 4:16:55 AM.
This article is licensed under a Creative Commons Attribution-NonCommercial 3.0 Unported Licence.

1. Introduction

CO_2 catalytic conversion is a consolidated approach for the sustainable production of value-added commodities and fuels, as well as a viable solution to mitigating carbon footprints and achieve carbon neutrality to face with global warming.[1,2] Among Carbon Capture and Utilization (CCU) technologies, CO_2 electrochemical reduction (CO_2RR) preferably combined with the use of renewable electricity sources is steadily attracting the interest of the catalysis community. Consequently, the development of efficient, sustainable, and inexpensive electrocatalytic systems is becoming a major challenge in the field.[3–6] Non-noble transition metal-based catalysts on carbon supports retain a dominant position in the technology devoted to electrocatalyst design and synthesis. Indeed, the generally cheap and Earth-abundant nature of the former combined with the inherent thermal stability, good electrical conductivity and easy chemico-physical tunability of the latter offer several opportunities for improving the catalytic performance of the resulting hybrids. Recent progresses in controlling the electronic surface properties of carbon-based networks have also endowed them with a role that looks beyond that of common and innocent carriers for a metal active phase.[1,7] Among transition metals, nickel is regarded as a valuable alternative to benchmark noble metal-based electrocatalysts for the CO_2RR (*i.e.*, Au, Pd and Ag).[8–12] On the other hand, in aqueous electrolytes,[13] nickel retains its well-known tendency to promote the competitive Hydrogen Evolution Reaction (HER). To date, mitigation of such a side process has been achieved through the adoption of synthetic strategies for tighter control over the electronic properties at metal active sites, *e.g.*, the synthesis of Ni–N–C single-atom catalysts (SACs)[14–17] and Ni@$C_{graphitic}$ core–shell-like particles.[13,18–20] In spite of promising electrochemical outcomes, Ni SACs as well as Ni@C core–shell par-

[a]*Institute of Chemistry of OrganoMetallic Compounds, ICCOM-CNR and Consorzio INSTM, Via Madonna del Piano, 10-50019, Sesto F.no, Florence, Italy. E-mail: giulia.tuci@iccom.cnr.it, giuliano.giambastiani@unifi.it*
[b]*Department of Chemistry "Giacomo Ciamician", University of Bologna, Via Piero Gobetti 85, 40129 Bologna, Italy. E-mail: g.valenti@unibo.it*
[c]*Institute of Chemistry of OrganoMetallic Compounds, ICCOM-CNR, Via G. Moruzzi, 1-56124 Pisa, Italy*
[d]*University of Florence, Department of Chemistry "U. Schiff" - DICUS – and INSTM Research Unit, Via della Lastruccia 3-13, 50019 Sesto Fiorentino, FI, Italy*
[e]*Center for Sustainable Future Technologies, Fondazione Istituto Italiano di Tecnologia, Via Livorno 60, Torino, 10144, Italy*
[f]*Institute of Condensed Matter Chemistry and Technologies for Energy, ICMATE-CNR, 35127 Padova, Italy*
[g]*Center for Chemical Catalysis – C3, Alma Mater Studiorum – Università di Bologna, Via Gobetti 85, 40129 Bologna, Italy*
[h]*Dalian National Laboratory for Clean Energy (DNL), Dalian Institute of Chemical Physics, Chinese Academy of Science, 457 Zhongshan Road, 116023 Dalian, China*
† Electronic supplementary information (ESI) available. See DOI: https://doi.org/10.1039/d4nr05259e

This journal is © The Royal Society of Chemistry 2025

Open Access Article. Published on 27 February 2025. Downloaded on 1/18/2026 4:16:55 AM. This article is licensed under a Creative Commons Attribution-NonCommercial 3.0 Unported Licence.

ticles still face technical limitations that concretely hamper their widespread application beyond that of their fundamental use on lab-scale setups.[19,21,22]

Traditional CO_2RR catalysts made of Ni NPs on carbon-based carriers exhibit moderate to good CO_2-to-CO conversion rates compared to their Ni-SACs or Ni@C counterparts.[18,21,23–25] Gu and co-workers have recently reported on the key size dependence of supported Ni NPs on N-doped carbon with respect to the CO faradaic efficiency (FE_{CO}) of their electrocatalysts. They showed that the larger the size of supported Ni NPs, the higher the contribution of the undesired HER process.[24] Alternative $2e^-$ reduction pathways to HCOOH are even rarer with nickel NP-based electrocatalysts. To the best of our knowledge, only less conventional nickel hybrids such as Ni SACs[26] or structurally well-confined Ni particles in the cavity of carbon shells[27] behave as active electrochemical systems for CO_2-to-formate reduction. On the other hand, bare C-carriers preferably selected from the series of lightweight (*i.e.*, N) hetero-doped C-networks have emerged as non-innocent and metal-free players for the selective electrochemical process.[28,29] The easy tuning of their chemical composition, morphology, and surface electronic properties has paved the way for the development of highly versatile CO_2RR organocatalysts for process intensification as well as for control over the CO_2 activation/reduction pathway.

Our team has recently described the use of a special class of N-rich C-nanoarchitectures (Covalent Triazine Frameworks, CTFs) characterized by high permanent porosity and thermochemical stability as robust metal-free systems with superior CO_2RR selectivity towards the challenging CO_2-to-HCOOH electroreduction.[30] The study witnesses the high versatility of a class of porous organic polymers,[31,32] whose field of application already includes a broad series of cases ranging from gas storage and separation,[31,33,34] energy storage and conversion[35] to heterogeneous catalysis.[36–39] Selected contributions from the literature have already documented the advantages arising from the use of highly electron-enriched C-networks (*i.e.*, N-doped) for the generation of virtually monodisperse metal-based hybrids, exhibiting superior robustness in terms of resistance to NPs leaching and sintering phenomena.[22,40]

Herein, we have applied the metal vapor synthesis (MVS) approach[41–44] as an alternative route to the more conventional impregnation/calcination/reduction sequence for the preparation of a Ni/CTF^{ph} hybrid starting from the same covalent triazine framework[30,32] that we recently employed as an effective and metal-free electrocatalyst for the almost chemoselective CO_2-to-HCOOH electroreduction ($FE_{HCOOH} \approx 66\%$) at moderate reducing potentials (*i.e.*, −0.4 V *vs.* RHE).[30] The MVS method for metal active-phase deposition has allowed for the preparation of a hybrid sample, characterized by ultrasmall (~2.2 nm) and almost monodisperse Ni NPs, while reducing as much as possible any thermo-chemical stress on the underlying carbonaceous support. As detailed below, the electrocatalytic performance of the hybrid has facilitated the unconventional CO_2-to-formate electroreduction even at low potentials (−0.3 V *vs.* RHE), while providing a highly selective system for syngas production ($CO : H_2 \approx 1 : 1$) at more reducing potentials (≥−0.6 V *vs.* RHE).

2. Materials and methods

2.1 Materials synthesis

CTF^{ph} was prepared according to literature procedures from 1,3-dicyanobenzene under ionothermal conditions in molten $ZnCl_2$.[30,32] Ni NPs were then deposited on CTF^{ph} by the MVS approach using a previously described reactor setup.[41] More specifically, Ni powder (0.35 g) was placed in an alumina crucible and subjected to resistive heating under low pressure (10^{-5} mbar), thereby generating nickel vapors that were co-condensed with mesitylene (100 mL) in a glass reactor chamber maintained at 77 K (liquid N_2). The reactor was then heated till the solid matrix reached its melting point (233 K). The as-obtained dark-brown Ni-mesitylene solution was collected in a Schlenk tube and maintained at 233 K. After ICP-OES analysis of the Ni-mesitylene solution, an appropriate amount of it was added to CTF^{ph} under an inert atmosphere and stirred at room temperature until the solution became colorless (about 12 h). After solvent removal, the solid Ni/CTF^{ph} underwent three washing cycles with *n*-pentane (3 × 10 mL) before being dried under reduced pressure until a constant weight was achieved.

2.2 Characterization

Transmission electron microscopy (TEM) analyses were performed on a ZEISS Libra 200FE instrument equipped with an in-column omega filter analyzer. Samples were dispersed in 2-propanol and sonicated for 15 min to obtain a homogeneous suspension, which was dropcast on a lacey carbon film Cu TEM grid. The samples were left to dry overnight before analyses. *N_2 physisorption* analyses were conducted on a Micromeritics ASAP2020 instrument after Ni/CTF^{ph} activation at 120 °C for 24 h under high vacuum. The specific surface area (SSA) was evaluated on the basis of the Brunauer–Emmett–Teller (BET) model while the pore size distribution was determined using a density functional theory (DFT) N_2-model for pores of slit geometry. *Powder X-ray diffraction* (PXRD) measurements were carried out in the 25–90° 2θ region on a Panalytical X'PERT PRO powder diffractometer equipped with a Ni-filtered diffracted beam, a PIXcel solid state detector and a sealed Cu Kα (λ = 1.5418 Å) X-ray tube. *X-ray photoelectron spectroscopy* (XPS) measurements were carried out in an ultra-high vacuum chamber system with a base pressure of $10^{-9}/10^{-10}$ mbar. A non-monochromatized Al Ka radiation source ($h\nu$ = 1486.6 eV, VSW-TA10) was used in combination with a hemispherical electron/ion energy analyzer (VSW-HA100 with a 16-channel detector). The operating power of the used X-ray source was maintained at 144 W (12 kV and 12 mA) and photoelectrons were collected normal to the sample surface, maintaining a fixed angle between the analyzer axis and the X-ray source at 54.5°. The spectra were acquired in fixed analyzer transmission (FAT) mode (pass energy of 44 eV). XPS spectra calibration was conducted by setting the C 1s sp^2 component to 285 eV. All spectra were analyzed using CASA XPS software[45] and a Shirley function was used to subtract the background. Peak fitting was accomplished with a combination of Gaussian and Lorentzian func-

Open Access Article. Published on 27 February 2025. Downloaded on 1/18/2026 4:16:55 AM. This article is licensed under a Creative Commons Attribution-NonCommercial 3.0 Unported Licence.

tions. *Inductively coupled plasma-optical emission spectrometer* (ICP-OES) analyses were conducted on an Optima 8000 ICP-OES (PerkinElmer) at 1500 W equipped with an S10 autosampler, a MiraMist nebulizer and a cyclonic chamber. Ni was examined at a wavelength of 231.604 nm. Before analyses, Ni/CTF^{ph} was heated in a 3 : 1 (v/v) HNO_3/H_2O_2 mixture at the boiling point until complete digestion. The solution was finally cooled and diluted with a 2% HNO_3 water solution. *Electrochemical characterization* was performed with an SP-300 bipotentiostat (*Biologic Instruments*) workstation, using a three-electrode system composed of a saturated calomel electrode (SCE), a Pt wire and a catalyst-modified glassy carbon electrode (GCE, d = 3 mm, and geometric area = 0.071 cm^2) as reference (RE), counter (CE) and working (WE) electrodes, respectively. Electrochemical characterization was performed in an Ar-saturated 0.1 M KOH electrolyte. To study its electrochemical properties, Ni-CTF^{ph} was suspended in EtOH and 0.5% Nafion with a concentration of 1.6 mg mL^{-1} and the homogeneous ink was drop-cast on a GC electrode (207 μg cm^{-2}). For all electrochemical measurements, the potentials were reported *versus* the RHE and corrected for ohmic drop.

2.3 CO_2RR measurements

An SP-300 potentiostat (*Biologic Instruments*) workstation and a custom-made electrochemical cell[46] with a three-electrode configuration were used to carry out the CO_2 reduction reaction (CO_2RR). The peculiar feature of this cell is that the WE is placed face-up at the bottom of the cell, and the CE (mesh Pt) is separated from the electrolyte by means of a porous frit. With this configuration, the gaseous products go directly towards the gas chromatograph (GC) for detection while liquid products cannot react with the CE. The reference electrode was an Ag/AgCl (LowProfile 3.5 mm OD from *PINE research*) equipped with a gel in place of the classical KCl solution. The gel and the ceramic porous frit guarantee low mobility of chloride ions, preventing their escape from the electrode with the consequent poisoning of the catalyst. The electrolysis tests were performed in a near-neutral bicarbonate buffer, $KHCO_3$ 0.5 M, pre-electrolysed before use to guarantee high purity. Pre-electrolysis was carried out on an Ar-saturated electrolyte in a two-electrode cell configuration, with a Pt wire and a Pt mesh as counter and working electrodes, respectively, for at least 16 h at 0.1 mA.[47] Blank tests on **1**, carried out under an inert atmosphere (Ar) and/or without the application of any external potential, have also been accomplished to exclude the presence of contaminants.

CO_2RR measurements were conducted with the same inks and material loading as those used for electrochemical characterization, except for the employment of a bigger working electrode (GCE, d = 18 mm, geometric surface area = 2.5 cm^2) in order to maximize reaction products concentration for a correct and reliable quantification. CO_2RR activity was evaluated by chronoamperometry (CA) for 1 hour and 26 minutes in CO_2-saturated electrolytes. The gaseous products were analyzed during measurements using an on-line gas chromatograph (GC) directly connecting the headspace of the electrochemical cell to the sample loop of the GC, while formic acid was detected by analysis of the liquid phase by Ionic Chromatography (IC) at the end of electrolysis. The gas phase quantification was carried out during the electrolysis with sampling every 20 minutes. The faradaic efficiency (FE) for the gas products of the CO_2RR was quantified using eqn (1):[48]

$$\mathrm{FE}\,(\%) = \frac{nF\varphi F_{\mathrm{m}}}{I} \quad (1)$$

where n is the number of electrons needed for the CO_2RR, F is the Faraday constant, φ is the volume fraction of the gas, I is the current and F_{m} is the molar Ar gas flow rate.

Analyses of liquid products were performed by means of a Metrohm model 850 Professional IC Ion Chromatograph equipped with a Metrosep A Supp 4-250/4.0 anion column and a conductivity detector (eluent: 0.5 mM H_2SO_4 with 15% acetone). FE for the formic acid products was calculated using eqn (2):

$$\mathrm{FE} = \frac{Q(\mathrm{HCOO^-})}{Q_{\mathrm{TOT}}} \times 100. \quad (2)$$

3. Results and discussion

CTF^{ph} was prepared and isolated according to literature procedures[32] before being employed as an N-enriched and highly mesoporous support for Ni(0) nanoparticles (NPs) (Scheme 1, see the Materials and methods section for details). Mesitylene-solvated Ni(0) NPs obtained by metal vapor synthesis (MVS)[41] were then highly dispersed on CTF^{ph} at room temperature to get the Ni/CTF^{ph} (**1**) catalyst with a nominal nickel content of 10 wt%. ICP analyses conducted on **1** have revealed an effective Ni content of 9.2 wt%. The as-synthesized Ni/CTF^{ph} (**1**) was then used in the catalytic runs without undergoing any further purification/activation steps.

The morphology of Ni NPs in **1** was first assessed by HR-TEM analysis. As Fig. 1A–C show, the sample presents a homogeneous and almost monodisperse distribution of NPs with a mean size of ≈ 2.2 nm throughout the whole scanned area (Fig. 1B) and well-resolved lattice fringes with a d-spacing of ≈ 0.208 nm ascribed to the (2 0 0) planes of NiO species (Fig. 1C). The uniform Ni NP dispersion on the CTF^{ph} surface along with the virtual absence of larger metal aggregates is ascribed to the combined action of N-doping[32] and the mild MVS conditions used for nickel deposition that exert a tight control over the ultimate morphology of the hybrid. The X-ray diffraction (XRD) pattern of **1** (Fig. 1D) presents very broad peaks, consistent with small-sized Ni(0)@Ni$^{2+/3+}$ core–shell-like particles, resulting from the rapid and spontaneous surface oxidation of the small Ni^0 NPs upon their exposure to air.

Accordingly, distinctive components at $2\theta \approx 37.2°$, 43.2°, 62.8°, 75.4°, 79.3°, $2\theta \approx 33.1°$, 38.5°, 52.1°, $2\theta \approx 31.9°$, 39.1°, 51.6°, 56.8° and $2\theta \approx 44.5°$, 76.3° were indexed to the (1 1 1), (2 0 0), (2 2 0), (3 1 1), (2 2 2) crystal planes of NiO species,[49,50] the (1 0 0), (1 0 1) (1 0 2) crystal planes of $Ni(OH)_2$,[51] the (0 0 2), (1 0 2), (1 1 2) (2 0 2) crystal planes of Ni_2O_3 [51] and the (1 1

 This journal is © The Royal Society of Chemistry 2025

Open Access Article. Published on 27 February 2025. Downloaded on 1/18/2026 4:16:55 AM.
This article is licensed under a Creative Commons Attribution-NonCommercial 3.0 Unported Licence.

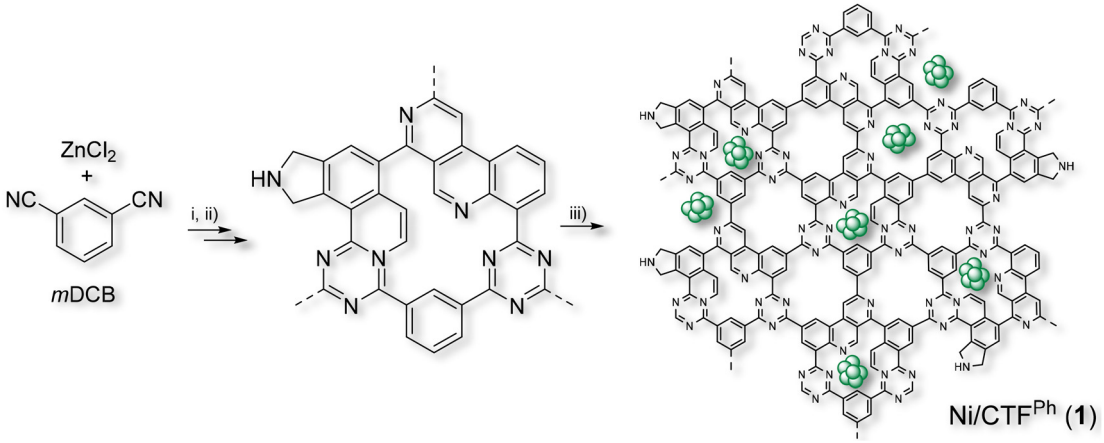

Scheme 1 Synthetic procedure for the preparation of Ni/CTF^{ph} (**1**). Reaction details: (i) $ZnCl_2$ melt mixture with *m*DCB under ionothermal conditions at (i) 400 °C for 10 h and (ii) 600 °C for an additional 10 h.[32] (iii) Deposition of Ni NPs by the MVS approach[44] (see the Materials and methods section for details).

1), (2 2 0) crystal planes of Ni(0),[40,52] respectively. A rough estimation of the metal NPs size has finally been derived from the application of the Scherrer equation[53] to the peak full width at half maximum (FWHM = 0.053 rad) of the NiO diffraction component at $2\theta \approx 62.8°$ [assigned to (2 2 0) Miller planes]. The calculated mean NP size (≈ 2.9 nm) was in good agreement with the size distribution estimated from TEM analysis. N_2 physisorption analyses of Ni/CTF^{ph} (**1**) and plain CTF^{ph} have been used to determine the textural properties of the former and the effect of Ni NP dispersion/confinement at the CTF^{ph} surface. As Fig. 2A shows, both samples present Type IV isotherm profiles along with an H2-type hysteresis loop typical of ink-bottle-shaped mesoporous networks.[54,55] The morphology of **1** largely reflects that of the plain CTF^{ph} support,[32] with micropores (micropore volume accounting for ~35% of the total pore volume) and little mesopores in the 2–6 nm range (Fig. 2B and Table S1†). From a comparison of the Ni/CTF^{ph} pore size distribution with that of the plain support (inset of Fig. 2B), it can be concluded that some of the small mesopores (3–5 nm mainly) were clogged by the metal NP deposit, while micropores remained almost unchanged before and after Ni NP loading. Accordingly, the SSA of **1** is slightly reduced to 1897 $m^2\ g^{-1}$ compared to that of its metal-free counterpart (CTF^{ph} = 2046 $m^2\ g^{-1}$, Table S1†).

Finally, XPS analysis has been carried out on Ni/CTF^{ph} (**1**) to provide additional details on the hybrid's chemical composition. XPS survey spectra confirmed the material purity and its expected elemental composition (C, N, O and Ni – Fig. S1†). The high-resolution XPS at the N 1s core region of Ni/CTF^{ph} (Fig. 2C) highlights the presence of the main signals of CTF samples [N-pyridinic (398.0 eV), N-pyrrolic (400.4 eV) and N-graphitic sites (401.5 eV)[30,56,57]] along with an additional component at 399.5 eV ascribed to the interaction/coordination between the N-enriched support and Ni NPs.[58]

A minor shoulder at 403.2 eV is finally attributed to the presence of N–O species likely due to moisture traces in the starting synthetic mixture.[59,60] In accordance with the information from XRD, the high-resolution Ni $2p^{3/2}$ XPS signal (Fig. 2D) presents two main components ascribable to Ni^{2+} and Ni^{3+} species.[44,61,62] The additional two peaks observed at higher BE values (red and blue empty curves in Fig. 2D) are ascribed to nickel satellites.[44]

Ni/CTF^{ph} (**1**) was electrochemically characterized by cyclic voltammetry (CV) in an Ar-saturated KOH 0.1 M solution using a three-electrode cell operated in the 0–1 V *vs*. RHE potential range. As expected, under alkaline electrolyte conditions and at open circuit potential, Ni^0 was promptly converted into α-$Ni(OH)_2$. The voltammetric peak ascribed to the reduction of α-$Ni(OH)_2$ overlaps with the side hydrogen evolution reaction (HER) (Fig. S2A†). In the reverse scan, hydrogen oxidation/desorption and Ni^0 oxidation to $Ni(OH)_2$ are observed. Clear (and reversible) oxidation peaks at 1.41 V ($E_{1/2}$ *vs*. RHE) measured at different scan rates are ascribed to Ni^{II}/Ni^{III} and Ni^{III}/Ni^{II} transitions, respectively (Fig. S2B†). The complete reversibility of these oxidation peaks confirms the excellent electronic conductivity of the catalytic hybrid, in particular between the CTF^{ph} support and the deposited metal active phase. These curves were finally employed to determine the electrochemically active area of **1**, whose value was fixed at 0.44 ± 0.08 cm^2.[63,64]

Ni/CTF^{ph} (**1**) was then scrutinized as a CO_2RR electrocatalyst under stationary conditions by chronoamperometry (CA) experiments carried out in a custom-made electrochemical cell[46] directly linked to a gas chromatograph for the on-line analysis of gaseous products. Liquid-phase products were analyzed at the end of the reduction process by means of ionic chromatography (IC). All electrochemical tests were performed in a CO_2-saturated $KHCO_3$ 0.5 M solution in the −0.3 to −0.8 V *vs*. RHE potential range and the electrochemical outcomes are summarized in the histograms in Fig. 3A. Fig. 3B shows the faradaic efficiency (FE) of any detectable CO_2 reduction products (including H_2 from the side HER) and total current

Open Access Article. Published on 27 February 2025. Downloaded on 1/18/2026 4:16:55 AM.
This article is licensed under a Creative Commons Attribution-NonCommercial 3.0 Unported Licence.

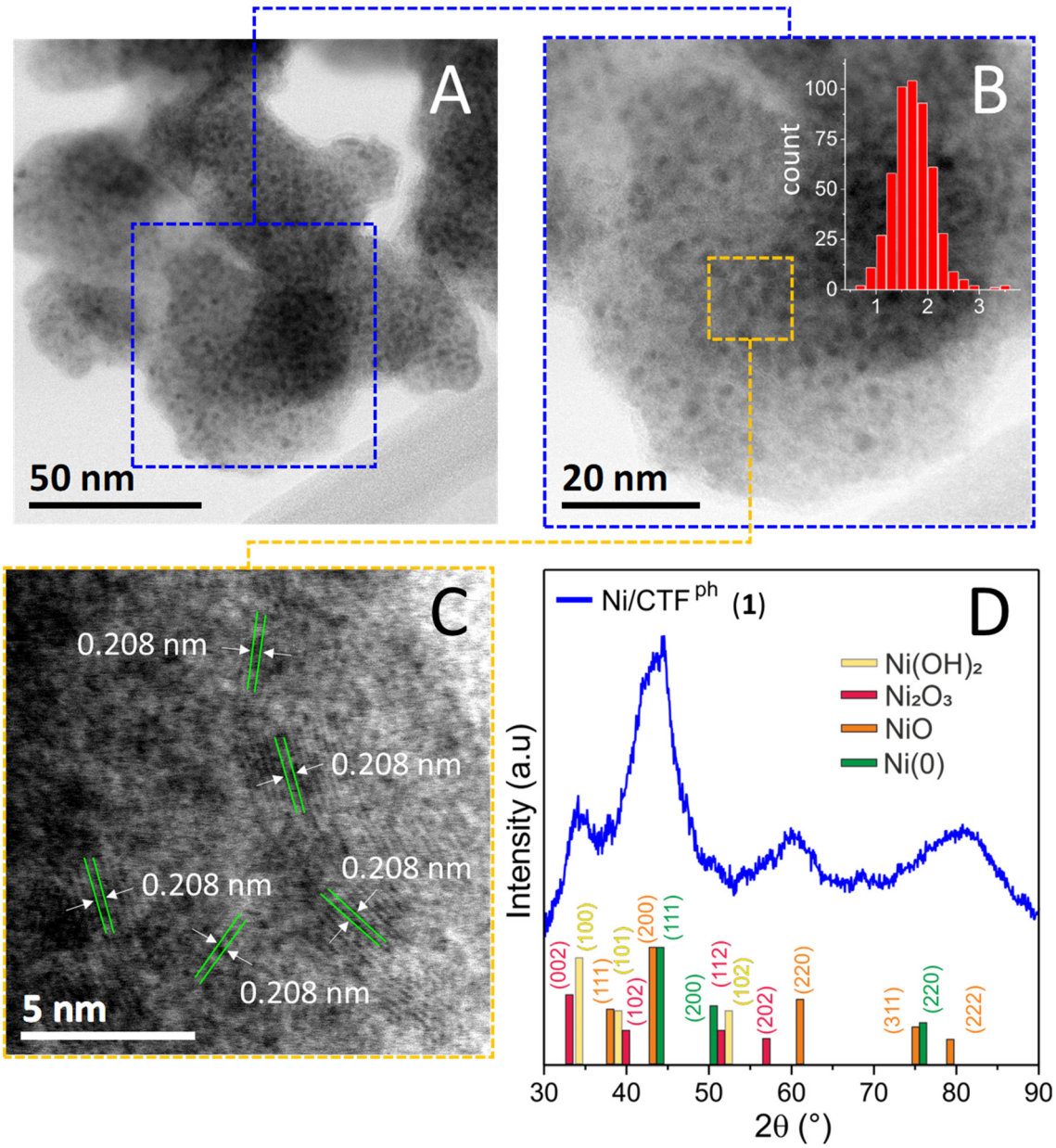

Fig. 1 (A–C) HR-TEM images of Ni/CTF^{ph} (**1**) at different magnifications and nickel particle size distribution measured over more than 100 NPs (red histograms in (B)). Fig. 1C shows well-resolved lattice fringes with a *d*-spacing of 0.208 nm corresponding to the (2 0 0) plane of NiO species. (D) XRD profile of **1** with related peak assignment.

density (j_{geom}), recorded at each potential value with the plain CTF^{ph} carrier as reproduced here from the literature[30] for comparison.

In contrast to the minor current density measured with metal-free CTF^{ph}, Ni/CTF^{ph} (**1**) exhibits an appreciable FE even at −0.3 V *vs.* RHE (Fig. 3A) along with the generation of HCOOH as the main 2e$^-$ CO_2 reduction product, not observed with the plain CTF^{ph} carrier at the same potential value. As mentioned above, formic acid is a rare CO_2RR product with Ni-based electrocatalysts at work.[22] It is typically obtained with less conventional systems such as Ni SACs or sub-nanometric Ni-clusters,[26] including structurally confined nickel NPs in mesoporous carbons (Ni@mC)[27] and is produced only at strong reducing potentials (*i.e.*, −0.8/−0.9 V *vs.* RHE). The virtual absence of HCOOH with the CTF^{ph} electrocatalyst at −0.3 V *vs.* RHE (Fig. 3B *vs.* Fig. 3A) leads us to postulate the rare action of Ni NPs as active sites in **1** for the generation of formic acid even at very moderate reducing potentials. It should be noticed that under mild reducing potentials (below −0.5 V *vs.* RHE) and pH values close to neutrality, nickel is prevalently available as Ni^{2+} (see also the Pourbaix diagram[65]). This feature well matches with what has been recently reported by Albero *et al.*,[26] who proposed the action of nickel in its higher oxidation states for the selective activation/reduction of

 This journal is © The Royal Society of Chemistry 2025

Open Access Article. Published on 27 February 2025. Downloaded on 1/18/2026 4:16:55 AM.
This article is licensed under a Creative Commons Attribution-NonCommercial 3.0 Unported Licence.

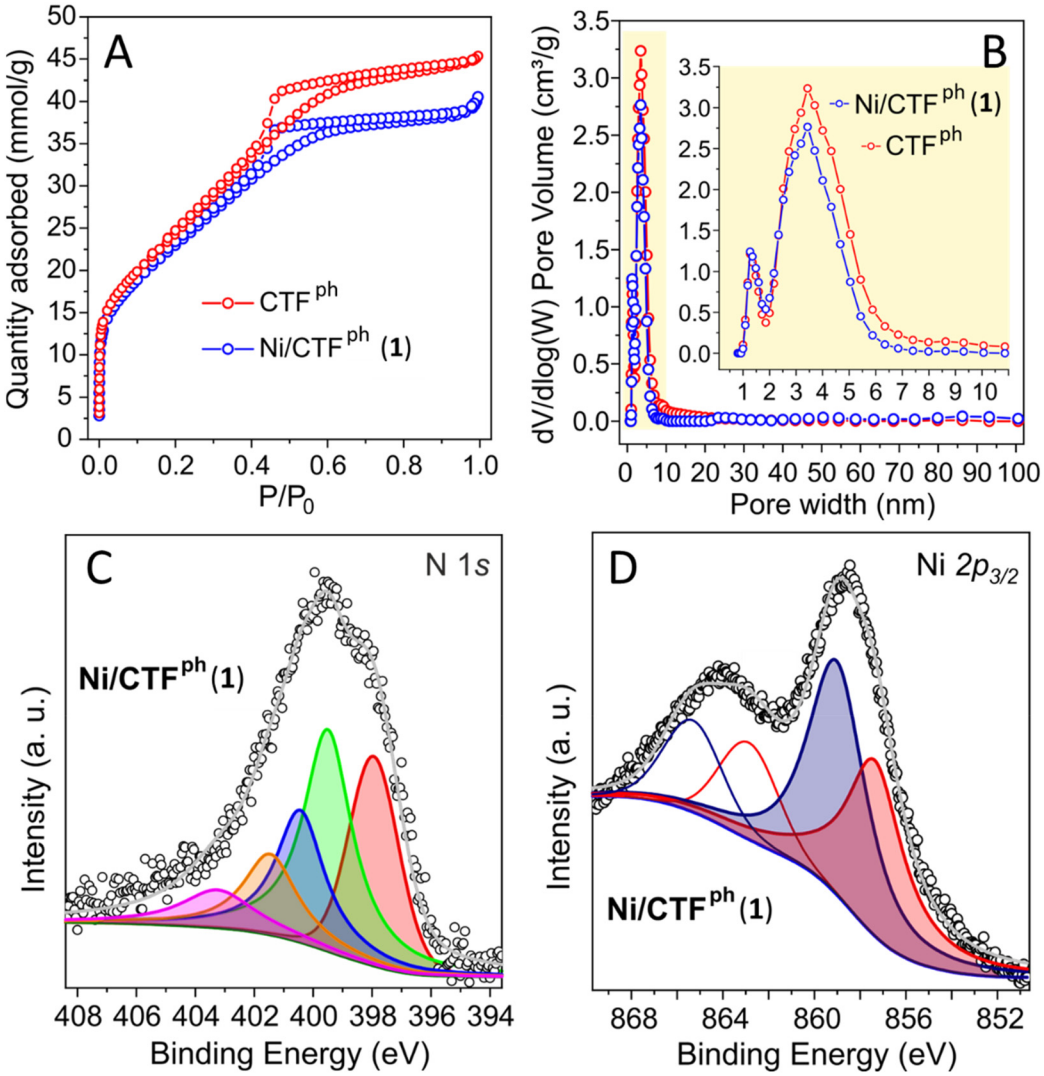

Fig. 2 (A) N_2 adsorption–desorption isotherms of CTF^{ph} (red curve) and Ni/CTF^{ph} (blue curve) recorded at the temperature of liquid N_2 along with (B) the respective pore-size distributions measured using the N_2-DFT model. Curves for CTF^{ph} as reported in ref. 30 are reported here for comparison. High-resolution XPS N 1s (C) and Ni $2p^{3/2}$ (D) core-level regions of Ni/CTF^{ph} (**1**) along with their relative fitting. Empty curves refer to satellite peaks.

CO_2 to formic acid. In addition, the morphological features of **1** are supposed to play a non-innocent role with respect to the unconventional FE_{HCOOH} measured with this electrocatalyst at work at low potential values. Ultrasmall Ni NPs produced by MVS accommodate prevalently within the small mesopores (3–5 nm) of the hosting CTF^{ph} matrix (see also Fig. 2B and Table S1†) and this evidence well aligns with space confinement criteria recently claimed by Chen *et al.*[27] with respect to the control of the process selectivity in CO_2-to-HCOOH reduction. Regardless of the origin (electronic, morphological or a combination thereof) of the HCOOH selectivity at low reducing potentials (−0.3 V *vs.* RHE), this evidence unambiguously implies the direct involvement of MVS-prepared Ni NPs with respect to the CO_2 activation/reduction pathway. Due to the low CO_2RR overpotentials explored in the study, *on-line* quantification of gaseous products (*i.e.*, H_2 and CO) is affected by a certain degree of inaccuracy. Typically, the lower the amount of gaseous products formed in the process, the higher the degree of inaccuracy in their *on-line* quantification and the estimation of the relative FE values. This is not the case for liquid products (*i.e.*, HCOOH) that accumulate throughout the whole electrolysis run before being quantified at the end of the CO_2RR with a net superior accuracy. As far as our electrocatalytic system is concerned, it is important to note that no other C-containing reduction products besides CO and HCOOH have ever been detected at the electrochemical cell outlet.

Higher reducing potentials (−0.4 V *vs.* RHE) translate into an FE_{HCOOH} of 23% with **1** (Fig. 3A), accompanied by a lower amount of CO as the more conventional $2e^-$ reduction product (FE_{CO} = 12%). The known performance of the plain CTF^{ph} network towards CO_2-to-formate conversion (Fig. 3B) does not

Open Access Article. Published on 27 February 2025. Downloaded on 1/18/2026 4:16:55 AM.
This article is licensed under a Creative Commons Attribution-NonCommercial 3.0 Unported Licence.

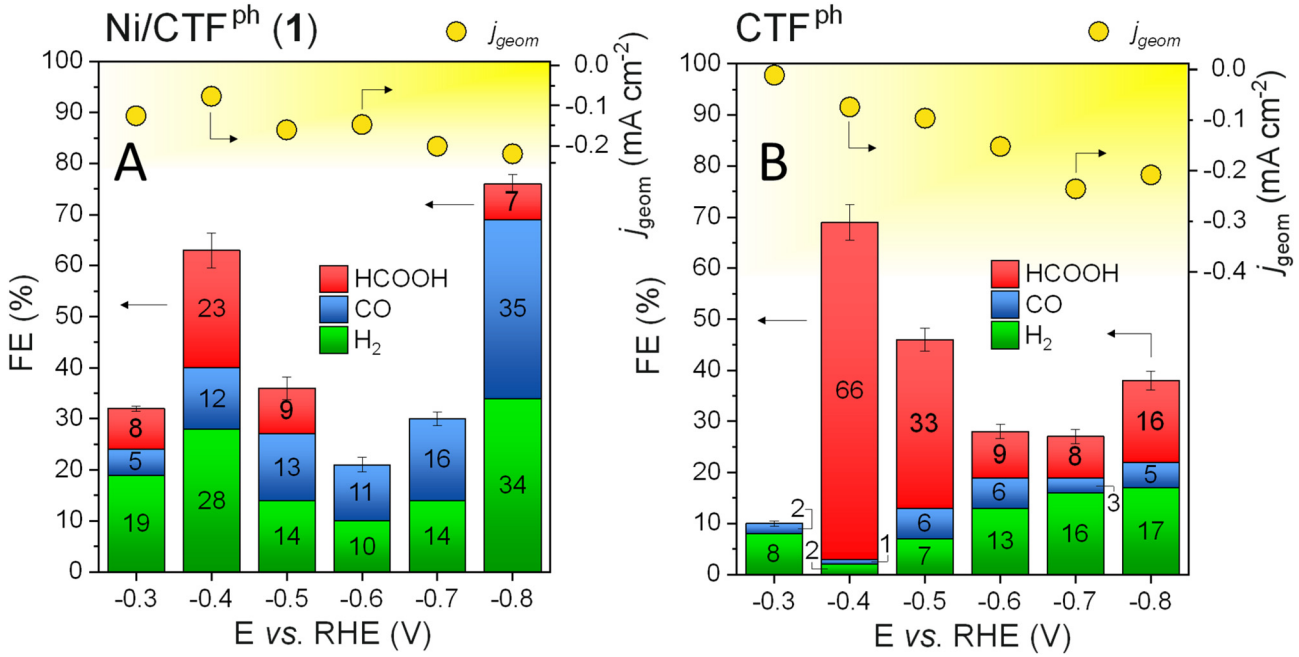

Fig. 3 (A) Faradaic Efficiency (FE_{HCOOH} – red, FE_{CO} – blue, and FE_{H_2} – green) and total (j_{geom} – yellow dots) current density values measured for Ni/CTF^{ph} (**1**) in the −0.3 to −0.8 V potential range *vs.* RHE. (B) FE_{HCOOH}, FE_{CO}, FE_{H_2} and total (j_{geom}) current density on the plain (metal-free) support from the literature[30] are reported here, with permission from the publisher, for comparison.

allow to discriminate between the nature of active sites (N-doped C-network *vs.* Ni NPs) really engaged in the CO_2 activation/reduction pathway and responsible for the observed selectivity at this potential value.

It should be noticed that at more reducing potentials, formate production with **1** decreases appreciably until being completely suppressed at −0.6 V *vs.* RHE. The FE_{HCOOH} measured on the plain CTF^{ph} (Fig. 3B) follows a similar trend, although maintaining itself constantly higher than FE_{CO} at the respective potential values. With **1**, the higher the applied reducing potential, the lower the contribution of the CTF nanocarrier to the CO_2 activation/reduction pathway. This occurs at those reducing potentials (above −0.5 V *vs.* RHE) and under almost neutral electrolyte conditions (like ours; pH ≈ 7.5) that guarantee the complete reduction of nickel species to their metallic Ni(0) form (Pourbaix diagrams). Accordingly, Ni(0) NPs become the main players in the CO_2-to-CO reduction process with an FE_{CO} up to 35% at −0.8 V *vs.* RHE (Fig. 3A). Noteworthy, at all potential values where Ni(0) NPs are claimed as the main active species (*i.e.*, −0.6 to −0.8 V *vs.* RHE), CO is accompanied by the simultaneous production of H_2 from the competitive HER in an almost constant H_2/CO ratio equal to one (Fig. 3A). Finally, at more reducing potentials, **1** re-exhibits the co-production of HCOOH (FE_{HCOOH} = 7% at −0.8 V *vs.* RHE), although to a lower extent with respect to CO and H_2 (Fig. 3A) but in line with the positive formate production trend measured on metal-free CTF^{ph} (Fig. 3B) at the respective potential value. HCOOH production at higher reducing potentials can then be ascribed to a competitive action of the CTF^{ph} carrier (Fig. 3B) in the CO_2RR, although a direct contribution of Ni NPs remains hard to be ruled out *a priori*. Indeed, Ni-based composites of the *state-of-the-art* (*i.e.*, Ni SACs and Ni@mC) start to co-produce HCOOH appreciably at these high reducing potentials.[26,27]

Finally, to check the stability of Ni/CTF^{ph} (**1**) under electrolysis conditions, we recovered it after CO_2RR and analysed it by HR TEM microscopy. As shown in Fig. S3,† no significant alterations in the statistical count of NPs were observed along with a similar mean size of the nickel phase (Fig. 1 and S3A *vs.* Fig. S3D†) for the two samples (fresh *vs.* used electrocatalyst **1**). ICP-OES quantification of leached nickel in the recovered liquid phase was found constantly below the technique's detection limit.

4. Conclusions

In summary, we described a mild thermochemical approach (MVS) for the preparation of a Ni/CTF^{ph} composite made of a highly dispersed nickel active phase at the outer surface of an already active and selective (metal-free) carrier (CTF) for the challenging $2e^-$ CO_2-to-HCOOH electroreduction. The exceptionally mild conditions of the MVS method for Ni NP deposition have allowed the chemical and morphological properties of the pristine CTF^{ph} to remain almost unchanged, while adding a further level of complexity (a new metal active phase) to the comprehension of the ultimate electrochemical performance of the composite in the CO_2RR.

Electrochemical studies have allowed us to speculate on the synergistic or exclusive action of the two potentially active

 This journal is © The Royal Society of Chemistry 2025

Open Access Article. Published on 27 February 2025. Downloaded on 1/18/2026 4:16:55 AM. This article is licensed under a Creative Commons Attribution-NonCommercial 3.0 Unported Licence.

phases (N-doped C-network *vs.* Ni NPs) in the CO_2RR. Nickel species in the form of small-sized Ni(0)@$Ni^{2+/3+}$ core–shell-like particles (low reducing potentials and almost neutral electrolyte conditions; pH ≈ 7.5, +0.3 V *vs.* RHE) promote CO_2-to-HCOOH electroreduction, where the plain CTF^{ph} carrier failed. To the best of our knowledge, this is a unique example of a classical Ni NP-based electrocatalyst for CO_2-to-formate production even at low reducing potentials. The higher the applied reducing potential, the lower the contribution of the CTF nanocarrier with respect to any CO_2 activation/reduction pathway. Although a dual contribution of the N-doped C-network and partially oxidized Ni NPs to FE_{HCOOH} at −0.4 to −0.5 V cannot be ruled out, more reducing potentials (above −0.5 V *vs.* RHE) and neutral electrolyte conditions make Ni(0) NPs the main (if not unique) players in CO_2-to-CO electroreduction along with simultaneous HER. The appearance of the HCOOH co-product at higher reducing potentials (−0.8 V *vs.* RHE, FE_{HCOOH} = 7%) is ascribed *a priori* to a competitive action of the underlying CTF^{ph} carrier. Anyhow, literature evidence of nickel-based electrocatalysts for HCOOH production operated at highly reducing potentials (*i.e.*, Ni SACs and Ni@mC) does not allow ruling out the direct action of Ni(0) NPs.

Author contributions

Conceptualization: G. T., G. V. and G. G.; methodology and its development: G. T., M. M. and C. E.; formal analysis: A. R., L. P., M. E., E. V., F. P. and Y. L.; investigation: M. M., L. P., C. E., G. T., G. V. and G. G. Data curation: G. T., M. M., M. E., E. V., C. E., G. V. and G. G.; writing – original draft: G. T., G. V. and G. G.; funding acquisition: G. G.

Data availability

The data supporting this article have been included as part of the ESI.†

Conflicts of interest

There are no conflicts to declare.

Acknowledgements

The Italian MUR through the PRIN2022 project "MATISSE – A "Molecular Lift" for the Control of the Metal Protrusion and Coordination Sphere in Single-Atom Catalysts for CO_2 Electroreduction" (2022K5SX27), "HYPOCOF – Hybrid Porous Materials for Eco-sustainable Catalytic Organic Processes" (B53C24005940006) and the European Union – NextGeneration EU through the Italian Ministry of Environment and Energy Security POR H2 AdP MMES/ENEA with the involvement of CNR and RSE, PNRR – Mission 2, Component 2, Investment 3.5 "Ricerca e sviluppo sull'idrogeno" (B93C22000630006) are kindly acknowledged for financial support. G. G. and Y. L. also thank the CAS President's International Fellowship Initiative (PIFI) program for supporting this research activity.

References

1 X. Long, F. Huang, Z. Yao, P. Li, T. Zhong, H. Zhao, S. Tian, D. Shu and C. He, Advancements in Electrocatalytic Nitrogen Reduction: A Comprehensive Review of Single-Atom Catalysts for Sustainable Ammonia Synthesis, *Small*, 2024, **20**, 2400551, DOI: **10.1002/smll.202400551**.

2 A. Saravanan, P. Senthil Kumar, D.-V. N. Vo, S. Jeevanantham, V. Bhuvaneswari, V. Anantha Narayanan, P. R. Yaashikaa, S. Swetha and B. Reshma, A comprehensive review on different approaches for CO_2 utilization and conversion pathways, *Chem. Eng. Sci.*, 2021, **236**, 116515, DOI: **10.1016/j.ces.2021.116515**.

3 D. Ewis, M. Arsalan, M. Khaled, D. Pant, M. M. Ba-Abbad, A. Amhamed and M. H. El-Naas, Electrochemical reduction of CO_2 into formate/formic acid: A review of cell design and operation, *Sep. Purif. Technol.*, 2023, **316**, 123811, DOI: **10.1016/j.seppur.2023.123811**.

4 B. Chang, H. Pang, F. Raziq, S. Wang, K.-W. Huang, J. Ye and H. Zhang, Electrochemical reduction of carbon dioxide to multicarbon (C_{2+}) products: challenges and perspectives, *Energy Environ. Sci.*, 2023, **16**, 4714–4758, DOI: **10.1039/D3EE00964E**.

5 K. Wiranarongkorn, K. Eamsiri, Y.-S. Chen and A. Arpornwichanop, A comprehensive review of electrochemical reduction of CO_2 to methanol: Technical and design aspects, *J. CO_2 Util.*, 2023, **71**, 102477, DOI: **10.1016/j.jcou.2023.102477**.

6 R. Küngas, Electrochemical CO_2 Reduction for CO Production: Comparison of Low- and High-Temperature Electrolysis Technologies, *J. Electrochem. Soc.*, 2020, **167**, 044508, DOI: **10.1149/1945-7111/ab7099**.

7 S. Liang, L. Huang, Y. Gao, Q. Wang and B. Liu, Electrochemical Reduction of CO_2 to CO over Transition Metal/N-Doped Carbon Catalysts: The Active Sites and Reaction Mechanism, *Adv. Sci.*, 2021, **8**, 2102886, DOI: **10.1002/advs.202102886**.

8 Y. H. Chen, C. W. Li and M. W. Kanan, Aqueous CO_2 Reduction at Very Low Overpotential on Oxide-Derived Au Nanoparticles, *J. Am. Chem. Soc.*, 2012, **134**, 19969–19972, DOI: **10.1021/ja309317u**.

9 B. Rosen, A. Salehi-Khojin, M. R. Thorson, W. Zhu, D. T. Whipple, P. J. A. Kenis and R. I. Masel, Ionic Liquid-Mediated Selective Conversion of CO_2 to CO at Low Overpotentials, *Science*, 2011, **334**, 643–644, DOI: **10.1126/science.120978**.

10 R. Kortlever, I. Peters, S. Koper and M. T. M. Koper, Electrochemical CO_2 Reduction to Formic Acid at Low Overpotential and with High Faradaic Efficiency on Carbon-Supported Bimetallic Pd-Pt Nanoparticles, *ACS Catal.*, 2015, **5**, 3916–3923, DOI: **10.1021/acscatal.5b00602**.

Open Access Article. Published on 27 February 2025. Downloaded on 1/18/2026 4:16:55 AM. This article is licensed under a Creative Commons Attribution-NonCommercial 3.0 Unported Licence.

11 R. E. Vos and M. T. M. Koper, Nickel as Electrocatalyst for CO(2) Reduction: Effect of Temperature, Potential, Partial Pressure, and Electrolyte Composition, *ACS Catal.*, 2024, **14**, 4432–4440, DOI: **10.1021/acscatal.4c00009**.

12 W. V. F. d. C. Batista, J. F. Coelho, W. L. de Oliveira, N. G. P. Filho, E. F. de Oliveira, T. d. S. da Cruz, H. S. T. da Silva, G. N. Marques, J. P. de Mesquita, R. F. B. de Souza and A. O. Neto, Nickel supported on polymeric graphitic carbon nitride for electrocatalytic in reduction of carbon dioxide, *J. CO_2 Util.*, 2023, **77**, 102614, DOI: **10.1016/j.jcou.2023.102614**.

13 R. Daiyan, X. Lu, X. Tan, X. Zhu, R. Chen, S. C. Smith and R. Amal, Antipoisoning Nickel-Carbon Electrocatalyst for Practical Electrochemical CO_2 Reduction to CO, *ACS Appl. Energy Mater.*, 2019, **2**, 8002–8009, DOI: **10.1021/acsaem.9b01470**.

14 K. Jiang, S. Siahrostami, T. Zheng, Y. Hu, S. Hwang, E. Stavitski, Y. Peng, J. Dynes, M. Gangisetty, D. Su, K. Attenkofer and H. Wang, Isolated Ni Single Atoms in Graphene Nanosheets for High-Performance CO_2 Reduction, *Energy Environ. Sci.*, 2018, **11**, 893–903, DOI: **10.1039/C7EE03245E**.

15 T. Moller, W. Ju, A. Bagger, X. Wang, F. Luo, T. Ngo Thanh, A. S. Varela, J. Rossmeisl and P. Strasser, Efficient CO_2 to CO Electrolysis on Solid Ni-N-C Catalysts at Industrial Current Densities, *Energy Environ. Sci.*, 2019, **12**, 640–647, DOI: **10.1039/C8EE02662A**.

16 D. Scarpa and M. Sarno, Single-Atom Catalysts for the Electro-Reduction of CO_2 to Syngas with a Tunable CO/H_2 Ratio: A Review, *Catalysts*, 2022, **12**, 275, DOI: **10.3390/catal12030275**.

17 C. Lu, J. Yang, S. Wei, S. Bi, Y. Xia, M. Chen, Y. Hou, M. Qiu, C. Yuan, Y. Su, F. Zhang, H. Liang and X. Zhuang, Atomic Ni Anchored Covalent Triazine Framework as High Efficient Electrocatalyst for Carbon Dioxide Conversion, *Adv. Funct. Mater.*, 2019, **29**, 1806884, DOI: **10.1002/adfm.201806884**.

18 W. Zheng, C. Guo, J. Yang, F. He, B. Yang, Z. Li, L. Lei, J. Xiao, G. Wu and Y. Hou, Highly active metallic nickel sites confined in N-doped carbon nanotubes toward significantly enhanced activity of CO_2 electroreduction, *Carbon*, 2019, **150**, 52–59, DOI: **10.1016/j.carbon.2019.04.112**.

19 M. Jia, C. Choi, T.-S. Wu, C. Ma, P. Kang, H. Tao, Q. Fan, S. Hong, S. Liu, Y.-L. Soo, Y. Jung, J. Qiu and Z. Sun, Carbon-supported Ni nanoparticles for efficient CO_2 electroreduction, *Chem. Sci.*, 2018, **9**, 8775–8780, DOI: **10.1039/C8SC03732A**.

20 T. Wang, J. Yang, J. Chen, Q. He, Z. Li, L. Lei, J. Lu, M. K. H. Leung, B. Yang and Y. Hou, Nitrogen-doped carbon nanotube-encapsulated nickel nanoparticles assembled on graphene for efficient CO_2 electroreduction, *Chin. Chem. Lett.*, 2020, **31**, 1438–1442, DOI: **10.1016/j.cclet.2020.04.056**.

21 Y. Cheng, S. Zhao, B. Johannessen, J.-P. Veder, M. Saunders, M. R. Rowles, M. Cheng, C. Liu, M. F. Chisolm, R. De Marco, H.-M. Cheng, S.-Z. Yang and S. P. Jiang, Atomically Dispersed Transition Metals on Carbon Nanotubes with Ultrahigh Loading for Selective Electrochemical Carbon Dioxide Reduction, *Adv. Mater.*, 2018, **30**, 1706287, DOI: **10.1002/adma.201706287**.

22 X.-H. Liu, X.-L. Jia, Y.-L. Zhao, R.-X. Zheng, Q.-L. Meng, C.-P. Liu, W. Xing and M.-L. Xiao, Recent advances in nickel-based catalysts for electrochemical reduction of carbon dioxide, *Adv. Sens. Energy Mater.*, 2023, **2**, 100073, DOI: **10.1016/j.asems.2023.100073**.

23 C. Zhao, X. Dai, T. Yao, W. Chen, X. Wang, J. Wang, J. Yang, S. Wei, Y. Wu and Y. Li, Ionic Exchange of Metal-Organic Frameworks to Access Single Nickel Sites for Efficient Electroreduction of CO_2, *J. Am. Chem. Soc.*, 2017, **139**, 8078–8081, DOI: **10.1021/jacs.7b02736**.

24 Z. Li, D. He, X. Yan, S. Dai, S. Younan, Z. Ke, X. Pan, X. Xiao, H. Wu and J. Gu, Size-Dependent Nickel-Based Electrocatalysts for Selective CO_2 Reduction, *Angew. Chem., Int. Ed.*, 2020, **59**, 18572–18577, DOI: **10.1002/anie.202000318**.

25 D. Tan, C. Cui, J. Shi, Z. Luo, B. Zhang, X. Tan, B. Han, L. Zheng, J. Zhang and J. Zhang, Nitrogen-carbon layer coated nickel nanoparticles for efficient electrocatalytic reduction of carbon dioxide, *Nano Res.*, 2019, **12**, 1167–1172, DOI: **10.1007/s12274-019-2372-1**.

26 E. Lepre, J. Heske, M. Nowakowski, E. Scoppola, I. Zizak, T. Heil, T. D. Kühne, M. Antonietti, N. Lopez-Salas and J. Albero, Ni-based electrocatalysts for unconventional CO_2 reduction reaction to formic acid, *Nano Energy*, 2022, **97**, 107191, DOI: **10.1016/j.nanoen.2022.107191**.

27 J. Du and A. Chen, Ni nanoparticles confined by yolk-shell structure of CNT-mesoporous carbon for electrocatalytic conversion of CO_2: Switching CO to formate, *J. Energy Chem.*, 2022, **70**, 224–229, DOI: **10.1016/j.jechem.2022.02.020**.

28 K. A. Adegoke and N. W. Maxakato, Electrochemical CO_2 conversion to fuels on metal-free N-doped carbon-based materials: functionalities, mechanistic, and technoeconomic aspects, *Mater. Today Chem.*, 2022, **24**, 100838, DOI: **10.1016/j.mtchem.2022.100838**.

29 I. M. Hasan, L. Peng, J. Mao, R. He, Y. Wang, J. Fu, N. Xu and J. Qiao, Carbon-based metal-free catalysts for electrochemical CO_2 reduction: Activity, selectivity, and stability, *Carbon Energy*, 2021, **3**, 24–49, DOI: **10.1002/cey2.87**.

30 M. Moro, G. Tuci, A. Rossin, C. Salvatici, E. Verlato, C. Evangelisti, F. Paolucci, G. Valenti, Y. Liu and G. Giambastiani, An ad-hoc Pyrolized Phoenix-like Covalent Triazine Framework for the Selective CO_2-to-Formate Electroreduction, *ACS Mater. Lett.*, 2024, **6**, 583–589, DOI: **10.1021/acsmaterialslett.3c01316**.

31 C. Krishnaraj, H. S. Jena, K. Leus and P. Van der Voort, Covalent triazine frameworks – a sustainable perspective, *Green Chem.*, 2020, **22**, 1038–1071, DOI: **10.1039/C9GC03482J**.

32 G. Tuci, M. Pilaski, H. Ba, A. Rossin, L. Luconi, S. Caporali, C. Pham-Huu, R. Palkovits and G. Giambastiani, Unraveling Surface Basicity and Bulk Morphology

 This journal is © The Royal Society of Chemistry 2025

Open Access Article. Published on 27 February 2025. Downloaded on 1/18/2026 4:16:55 AM. This article is licensed under a Creative Commons Attribution-NonCommercial 3.0 Unported Licence.

Relationship on Covalent Triazine Frameworks with Unique Catalytic and Gas Adsorption Properties, *Adv. Funct. Mater.*, 2017, **27**, 1605672, DOI: **10.1002/adfm.201605672**.

33 G. Tuci, A. Iemhoff, A. Rossin, D. Yakhvarov, M. F. Gatto, R. Balderas-Xicohténcatl, L. Zhang, M. Hirscher and R. Palkovits, Tailoring Morphological and Chemical Properties of Covalent Triazine Frameworks for dual CO_2 and H_2 Adsorption, *Int. J. Hydrogen Energy*, 2022, **47**, 8434–8445, DOI: **10.1016/j.ijhydene.2021.12.197**.

34 Q.-W. Deng, G.-Q. Ren, Y.-J. Li, L. Yang, S.-L. Zhai, T. Yu, L. Sun, W.-Q. Deng, A. Li and Y.-H. Zhou, Hydrogen and CO_2 storage in high surface area covalent triazine–based frameworks, *Mater. Today Energy*, 2020, **18**, 100506, DOI: **10.1016/j.mtener.2020.100506**.

35 Y. Zheng, N. A. Khan, X. Ni, K. A. I. Zhang, Y. Shen, N. Huang, X. Y. Kong and L. Ye, Emerging covalent triazine framework-based nanomaterials for electrochemical energy storage and conversion, *Chem. Commun.*, 2023, **59**, 6314–6334, DOI: **10.1039/D3CC00712J**.

36 Z. Qian, Z. J. Wang and K. A. I. Zhang, Covalent Triazine Frameworks as Emerging Heterogeneous Photocatalysts, *Chem. Mater.*, 2021, **33**, 1909–1926, DOI: **10.1021/acs.chemmater.0c04348**.

37 J. Artz, Covalent Triazine-based Frameworks-Tailor-made Catalysts and Catalyst Supports for Molecular and Nanoparticulate Species, *ChemCatChem*, 2018, **10**, 1753–1771, DOI: **10.1002/cctc.201701820**.

38 P. Puthiaraj, Y. R. Lee, S. Zhang and W. S. Ahn, Triazine-Based Covalent Organic Polymers: Design, Synthesis and Applications in Heterogeneous Catalysis, *J. Mater. Chem. A*, 2016, **4**, 16288–16311, DOI: **10.1039/C6TA06089G**.

39 D. Yadav, D. Subodh and S. K. Awasthi, Recent advances in the design, synthesis and catalytic applications of triazine-based covalent organic polymers, *Mater. Chem. Front.*, 2022, **6**, 1574–1605, DOI: **10.1039/D2QM00071G**.

40 M. V. Pagliaro, H. A. Miller, C. Evangelisti, M. Bellini, G. Tuci, C. Pham-Huu, G. Giambastiani, M. Marelli and F. Vizza, Synergy between Nickel Nanoparticles and N-Enriched Carbon Nanotubes Enhances Alkaline Hydrogen Oxidation and Evolution Activity, *ACS Appl. Nano Mater.*, 2021, **4**, 3586–3596, DOI: **10.1021/acsanm.1c00118**.

41 E. Pitzalis, R. Psaro and C. Evangelisti, From metal vapor to supported single atoms, clusters and nanoparticles: Recent advances to heterogeneous catalysts, *Inorg. Chim. Acta*, 2022, **533**, 120782, DOI: **10.1016/j.ica.2021.120782**.

42 P. Tegeder, M. Marelli, M. Freitag, L. Polito, S. Lamping, R. Psaro, F. Glorius, B. J. Ravoo and C. Evangelisti, Metal vapor synthesis of ultrasmall Pd nanoparticles functionalized with N-heterocyclic carbenes, *Dalton Trans.*, 2018, **47**, 12647–12651, DOI: **10.1039/C8DT02535E**.

43 L. A. Aronica, A. M. Caporusso, G. Tuci, C. Evangelisti, M. Manzoli, M. Botavina and G. Martra, Palladium nanoparticles supported on Smopex® metal scavengers as catalyst for carbonylative Sonogashira reactions: Synthesis of a, b-alkynyl ketones, *Appl. Catal., A*, 2014, **480**, 1–9, DOI: **10.1016/j.apcata.2014.04.029**.

44 E. Punzi, X. T. Nguyen, E. Pitzalis, A. Mandoli, M. Onor, M. Marelli, L. Poggini, G. Tuci, G. Giambastiani and C. Evangelisti, Ultrasmall Nickel Nanoparticles on a Covalent Triazine Framework for Ammonia Borane Hydrolysis and Transfer Hydrogenation of Nitroaromatics, *ACS Appl. Nano Mater.*, 2024, **7**, 6916–6926, DOI: **10.1021/acsanm.3c05844**.

45 N. Fairley, V. Fernandez, M. Richard-Plouet, C. Guillot-Deudon, J. Walton, E. Smith, D. Flahaut, M. Greiner, M. Biesinger, S. Tougaard, D. Morgan and J. Baltrusaitis, Systematic and collaborative approach to problem solving using X-ray photoelectron spectroscopy, *Appl. Surf. Sci.*, 2021, **5**, 100112, DOI: **10.1016/j.apsadv.2021.100112**.

46 E. Verlato, S. Barison, Y. Einaga, S. Fasolin, M. Musiani, L. Nasi, K. Natsui, F. Paolucci and G. Valenti, CO_2 reduction to formic acid at low overpotential on BDD electrodes modified with nanostructured CeO_2, *J. Mater. Chem. A*, 2019, **7**, 17896–17905, DOI: **10.1039/C9TA01000A**.

47 Y. Hori, H. Konishi, T. Futamura, A. Murata, O. Koga, H. Sakurai and K. Oguma, "Deactivation of copper electrode" in electrochemical reduction of CO_2, *Electrochim. Acta*, 2005, **50**, 5354–5369, DOI: **10.1016/j.electacta.2005.03.015**.

48 R. Kas, R. Kortlever, A. Milbrat, M. T. M. Koper, G. Mul and J. Baltrusaitis, Electrochemical CO_2 reduction on Cu_2O-derived copper nanoparticles: controlling the catalytic selectivity of hydrocarbons, *Phys. Chem. Chem. Phys.*, 2014, **16**, 12194–12201, DOI: **10.1039/C4CP01520G**.

49 H. Qiao, Z. Wei, H. Yang, L. Zhu and X. Yan, Preparation and Characterization of NiO Nanoparticles by Anodic Arc Plasma Method, *J. Nanomater.*, 2009, 795925, DOI: **10.1155/2009/795928**.

50 B. Kavitha, M. Nirmala and A. Pavithra, Annealing effect on nickel oxide nanoparticles synthesized by sol-gel method, *WSN*, 2016, **52**, 118–129.

51 J. J. de la Cruz-Cruz, M. A. Domínguez-Crespo, E. Ramírez-Meneses, A. M. Torres-Huerta, S. B. Brachetti-Sibaja, A. E. Rodríguez-Salazar, E. Pastor and L. E. González-Sánchez, Data supporting the in situ synthesis by organometallic method of Vulcan supported PdNi nanostructures for hydrogen evolution reaction in alkaline solution, *Data Brief*, 2022, **42**, 108256, DOI: **10.1016/j.dib.2022.108256**.

52 W. Wang, C. Duong-Viet, H. Ba, W. Baaziz, G. Tuci, S. Caporali, L. Nguyen-Dinh, O. Ersen, G. Giambastiani and C. Pham-Huu, Nickel Nanoparticles Decorated Nitrogen-Doped Carbon Nanotubes (Ni/N-CNT); a Robust Catalyst for the Efficient and Selective CO_2 Methanation, *ACS Appl. Energy Mater.*, 2019, **2**, 1111–1120, DOI: **10.1021/acsaem.8b01681**.

53 R. Jenkins and R. L. Snyder, *Introduction to X-Ray Powder Diffractometry*, John Wiley & Sons Inc., 1996, pp. 89–91.

54 K. S. W. Sing, D. H. Everett, R. A. W. Haul, L. Moscou, R. A. Pierotti and J. Rouquérol, Reporting Physisorption Data for Gas/Solid Systems with Special Reference to the

Open Access Article. Published on 27 February 2025. Downloaded on 1/18/2026 4:16:55 AM.
This article is licensed under a Creative Commons Attribution-NonCommercial 3.0 Unported Licence.

Determination of Surface Area and Porosity, *Pure Appl. Chem.*, 1985, **57**, 603–619, DOI: **10.1351/pac198557040603**.

55 S.-S. Chang, B. Clair, J. Ruelle, J. Beauchene, F. Di Renzo, F. Quignard, G.-J. Zhao, H. Yamamoto and J. Gril, Mesoporosity as a new parameter for understanding tension stress generation in trees, *J. Exp. Bot.*, 2009, **60**, 3023–3030, DOI: **10.1093/jxb/erp133**.

56 A. Bhunia, V. Vasylyeva and C. Janiak, From a supramolecular tetranitrile to a porous covalent triazine-based framework with high gas uptake capacities, *Chem. Commun.*, 2013, **49**, 3961–3963, DOI: **10.1039/C3CC41382A**.

57 K. Wang, H. Huang, D. Liu, C. Wang, J. Li and C. Zhong, Covalent Triazine-Based Frameworks with Ultramicropores and High Nitrogen Contents for Highly Selective CO_2 Capture, *Environ. Sci. Technol.*, 2016, **50**, 4869–4876, DOI: **10.1021/acs.est.6b00425**.

58 S. Öztürk, Y.-X. Xiao, D. Dietrich, B. Giesen, J. Barthel, J. Ying, X.-Y. Yang and C. Janiak, Nickel nanoparticles supported on a covalent triazine framework as electrocatalyst for oxygen evolution reaction and oxygen reduction reactions, *Beilstein J. Nanotechnol.*, 2020, **11**, 770–781, DOI: **10.3762/bjnano.11.62**.

59 G. Tuci, A. Iemhoff, H. Ba, L. Luconi, A. Rossin, V. Papaefthimiou, R. Palkovits, J. Artz, C. Pham-Huu and G. Giambastiani, Playing with covalent triazine framework tiles for improved CO_2 adsorption properties and catalytic performance, *Beilstein J. Nanotechnol.*, 2019, **10**, 1217–1227, DOI: **10.3762/bjnano.10.121**.

60 S. Mukherjee, M. Das, A. Manna, R. Krishna and S. Das, Newly designed 1,2,3-triazole functionalized covalent triazine frameworks with exceptionally high uptake capacity for both CO_2 and H_2, *J. Mater. Chem. A*, 2019, **7**, 1055–1068, DOI: **10.1039/C8TA08185A**.

61 Q. Chen, Y. Yu, S. Zhou, L. Sha, G. Zhuang, P. Wang and X. Han, Electrocatalytic Overall Water Splitting Induced by Surface Reconstruction of an Iron-Modified Ni_2P/Ni_5P_4 Heterojunction Array Encapsulated into a N-Doped Carbon Layer, *Inorg. Chem.*, 2023, **62**, 6518–6526, DOI: **10.1021/acs.inorgchem.3c00703**.

62 N. Kitchamsetti, M. S. Ramteke, S. R. Rondiya, S. R. Mulani, M. S. Patil, R. W. Cross, N. Y. Dzade and R. S. Devan, DFT and experimental investigations on the photocatalytic activities of NiO nanobelts for removal of organic pollutants, *J. Alloys Compd.*, 2021, **855**, 157337, DOI: **10.1016/j.jallcom.2020.157337**.

63 E. Verlato, S. Cattarin, N. Comisso, A. Gambirasi, M. Musiani and L. Vazquez-Gomez, Preparation of Pd-Modified Ni Foam Electrodes and Their Use as Anodes for the Oxidation of Alcohols in Basic Media, *Electrocatalysis*, 2012, **3**, 48–58, DOI: **10.1007/s12678-011-0075-9**.

64 Y.-Y. Lou, W. He, E. Verlato, M. Musiani, D. Floner, F. Fourcade, A. Amrane, C. Li, Z.-Q. Tian, O. Merdrignac-Conanec, N. Coulon and F. Geneste, Ni-coated graphite felt modified with Ag nanoparticles: A new electrode material for electro-reductive dechlorination, *J. Electroanal. Chem.*, 2019, **849**, 113357, DOI: **10.1016/j.jelechem.2019.113357**.

65 L.-F. Huang, M. J. Hutchison, R. J. Santucci, J. R. Scully and J. M. Rondinelli, Improved Electrochemical Phase Diagrams from Theory and Experiment: The Ni-Water System and Its Complex Compounds, *J. Phys. Chem. C*, 2017, **121**, 9782–9789, DOI: **10.1021/acs.jpcc.7b02771**.

This journal is © The Royal Society of Chemistry 2025